ADVANCED MATERIALS
www.advmat.de

Room-Temperature Antisymmetric Magnetoresistance in van der Waals Ferromagnet Fe_3GaTe_2 Nanosheets

Guojing Hu, Hui Guo, Senhao Lv, Linxuan Li, Yunhao Wang, Yechao Han, Lulu Pan, Yulan Xie, Weiqi Yu, Ke Zhu, Qi Qi, Guoyu Xian, Shiyu Zhu, Jinan Shi, Lihong Bao, Xiao Lin, Wu Zhou, Haitao Yang,* and Hong-jun Gao**

Van der Waals (vdW) ferromagnetic materials have emerged as a promising platform for the development of 2D spintronic devices. However, studies to date are restricted to vdW ferromagnetic materials with low Curie temperature (T_c) and small magnetic anisotropy. Here, a chemical vapor transport method is developed to synthesize a high-quality room-temperature ferromagnet, Fe_3GaTe_2 (c-Fe_3GaTe_2), which boasts a high T_c = 356 K and large perpendicular magnetic anisotropy. Due to the planar symmetry breaking, an unconventional room-temperature antisymmetric magnetoresistance (MR) is first observed in c-Fe_3GaTe_2 devices with step features, manifesting as three distinctive states of high, intermediate, and low resistance with the sweeping magnetic field. Moreover, the modulation of the antisymmetric MR is demonstrated by controlling the height of the surface steps. This work provides new routes to achieve magnetic random storage and logic devices by utilizing the room-temperature thickness-controlled antisymmetric MR and further design room-temperature 2D spintronic devices based on the vdW ferromagnet c-Fe_3GaTe_2.

1. Introduction

The emergence of van der Waals (vdW) ferromagnetic materials provides an unprecedented platform for the study of fundamental 2D magnetism and the manipulation of spin-related phenomena, paving the way for promising 2D spintronics in low-power electronics.[1,3] To date, various 2D ferromagnetic materials have been identified, but the low Curie temperature (T_c) of most ferromagnetic materials limits their application in spintronic devices.[2,4] Although some room-temperature ferromagnetic materials, such as Fe_5GeTe_2[5] and $CrTe_2$,[6] have been reported, their practical application in 2D spintronics is hindered by issues like instability and small magnetic anisotropy.[7] Therefore, the exploration of new room-temperature 2D ferromagnetic materials with excellent magnetic properties is crucial for the development of 2D spintronic devices.

The research of magnetoresistance (MR) in 2D ferromagnetic materials has been an important topic in the development of 2D spintronics.[7,8] Devices based on 2D giant magnetoresistance and tunnel magnetoresistance have been developed, and their applications have been actively explored.[9] These devices operate by leveraging the symmetric high- and low-resistance states, which result from the parallel and antiparallel arrangement of magnetic moments in two ferromagnetic layers during sweeping the magnetic field.[10] Unlike these symmetry MR systems, an unusual antisymmetric MR has been observed in several 2D systems, including (Bi, Sb)$_2Te_3$-based topological magnetic heterostructures,[11] Fe_3GeTe_2-based magnetic heterostructures,[12] and single Fe_3GeTe_2 nanosheets with planar symmetry breaking.[13] The antisymmetric MR exhibits three states of resistance – high, intermediate, and low – which can be encoded as "−1," "0," "1" to achieve magnetic random storage and logic circuits. However, the maximum temperatures at which antisymmetric MR appears in these systems can only reach 150 K,[13a] significantly below the room temperature, thereby limiting its practical applications in 2D spintronic devices.

In this paper, we successfully synthesized high-quality ferromagnetic metal c-Fe_3GaTe_2 with a high T_c up to 356 K and strong perpendicular magnetic anisotropy using the chemical vapor transport (CVT) method. We report the observation of room-temperature antisymmetric MR in a c-Fe_3GaTe_2 nanosheet featuring a step edge that breaks the planar

G. Hu, H. Guo, S. Lv, Y. Wang, Y. Han, L. Pan, Y. Xie, W. Yu, K. Zhu, Q. Qi, G. Xian, S. Zhu, L. Bao, H. Yang, H.-jun Gao
Beijing National Center for Condensed Matter Physics and Institute of Physics
Chinese Academy of Sciences
Beijing 100190, P. R. China
E-mail: htyang@iphy.ac.cn; hjgao@iphy.ac.cn

H. Guo, S. Lv, L. Li, Y. Wang, Y. Han, K. Zhu, Q. Qi, G. Xian, S. Zhu, J. Shi, L. Bao, X. Lin, W. Zhou, H. Yang, H.-jun Gao
School of Physical Sciences
University of Chinese Academy of Sciences
Beijing 100049, China
E-mail: wuzhou@ucas.ac.cn

L. Bao, H. Yang, H.-jun Gao
Songshan Lake Materials Laboratory
Dongguan, Guangdong 523808, China

The ORCID identification number(s) for the author(s) of this article can be found under https://doi.org/10.1002/adma.202403154

DOI: 10.1002/adma.202403154

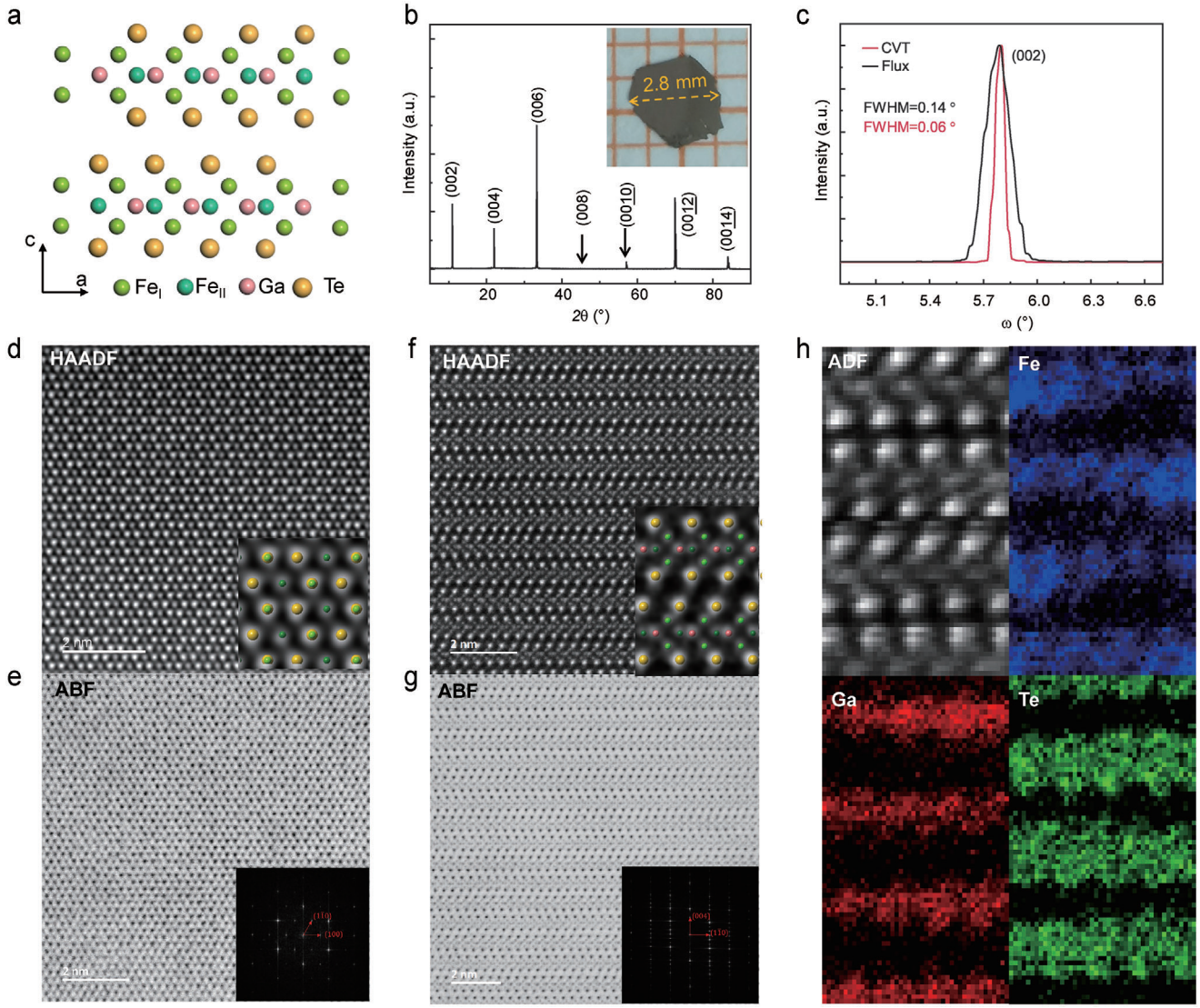

Figure 1. a) Crystal atomic structure of the c-Fe_3GaTe_2 *ac*-plane. b) X-ray diffraction data of a single crystal c-Fe_3GaTe_2 grown by CVT. The inset shows an image of the as-grown c-Fe_3GaTe_2. c) Rocking curves of the as-grown c-Fe_3GaTe_2 and f-Fe_3GaTe_2. d,e) STEM-HAADF and STEM-ABF images of the c-Fe_3GaTe_2 in the *ab*-plane. The corresponding atomic model and FFT pattern are shown in the insets of (d) and (e), respectively. f,g) STEM-HAADF and STEM-ABF images of the c-Fe_3GaTe_2 in the *ac*-plane. The corresponding atomic model and FFT pattern are shown in the insets of (f) and (g), respectively. h) STEM–EELS elemental mapping of Fe (blue), Ga (red), Te (green), presented alongside the concurrent ADF of the *ac*-plane.

symmetry. This phenomenon is attributed to the emergence of a circulating current near the boundaries of domain walls, driven by the unsynchronized magnetic switching in c-Fe_3GaTe_2 nanosheets of varying thicknesses. Importantly, we demonstrate that the magnitude of the antisymmetric MR can be modulated by changing the height of the surface steps between regions of different thicknesses. This room-temperature, thickness-adjustable antisymmetric MR offers new possibilities to achieve random storage and logic circuits in a simple 2D nanosheet without the need for complex device structures. Our findings underscore the potential of room-temperature ferromagnetic c-Fe_3GaTe_2 in the development of 2D spintronic devices.

2. Results and Discussion

2.1. High Quality of c-Fe_3GaTe_2 Crystals

As a vdW metallic ferromagnetic material, Fe_3GaTe_2 crystallizes into *P*63/*mmc* space group with a Fe/FeGa/Fe heterometallic slab sandwiched between two Te layers, forming a monolayer of Fe_3GaTe_2, which is stacked along the *c*-axis (**Figure 1a**). Hexagonal-shaped crystal c-Fe_3GaTe_2 with an average size of 2.8 mm (inset of Figure 1b) is synthesized by a CVT method. This synthesis method yields crystals of superior quality compared to those synthesized by the reported flux method (f-Fe_3GaTe_2).[14] As shown in Figure 1b, the X-ray diffraction (XRD)

pattern of c-Fe_3GaTe_2 only shows the characteristic diffraction peak of (00l), whose JCPDS pattern numbers can refer to that of $Fe_{0.6}Ni_{2.4}GaTe_2$ (04-024-6574). By contrast, XRD pattern of f-Fe_3GaTe_2 exhibits not only the characteristic diffraction peak of (00l), but also an additional peak at 26°, attributed to the (111) diffraction of Ga_2Te_3 (JCPDS No.: 00-057-0364) (Figure S1a, Supporting Information). Moreover, the rocking curve of the (002) peak of c-Fe_3GaTe_2 possesses a full width at half peak(FWHM) of 0.06, which is significantly smaller than the 0.14 observed in f-Fe_3GaTe_2 (Figure 1c). The (0*kl*) plane diffraction pattern of c-Fe_3GaTe_2 shows much sharper diffraction spots, without any splitting and deformation, as compared to that of f-Fe_3GaTe_2 (Figure S2, Supporting Information). These results show that c-Fe_3GaTe_2 has much higher crystal quality than f-Fe_3GaTe_2.

Energy-dispersive X-ray spectroscopy (EDS) analysis of the c-Fe_3GaTe_2 nanosheets reveals an atomic ratio of Fe, Ga, and Te of 3.07:1:2.01, closely aligning with the stoichiometric ratio of 3:1:2 (Figure S3a, Supporting Information). In addition, EDS mappings, depicted in Figure S3b (Supporting Information), confirm a uniform distribution of Fe, Ga, and Te elements. The atomic structure and crystal quality of the as-synthesized c-Fe_3GaTe_2 crystal were further characterized using an aberration-corrected scanning transmission electron microscope (STEM). The STEM high-angle annular dark-field (HAADF) images, covering a large field of view, show no extended lattice defects throughout the entire area (Figure S4, Supporting Information). Figure 1d–g presents the atomic-resolution STEM-HAADF images alongside the simultaneously acquired annular bright-field (ABF) images of the crystals. These images are taken along the *c*-axis ([001] zone-axis, Figure 1d,e) and the *b*-axis ([110] zone-axis, Figure 1f,g), respectively, with the corresponding fast Fourier transformation (FFT) patterns shown in the insets. The HAADF images, in which the contrast depends approximately on the square of the atomic number (*Z*), help in distinguishing the spatial distribution of distinct elements based on the image intensity. The in-plane structure, observed along the *c*-axis (Figure 1d), clearly shows that each Fe atomic column is surrounded by six brighter atomic columns, comprising a mix of Te, Ga, and Fe, arranging into a honeycomb lattice, consistent with the overlaid in-plane atomic structural model (inset of Figure 1d). The HAADF (Figure 1f) and ABF images (Figure 1g) of the *ac*-plane reveal that each monolayer consists of Fe/FeGa/Fe triatomic layers sandwiched between two atomic layers of Te, again matching well with the atomic structure projected along the *b*-axis (inset of Figure 1f). Additionally, the core-loss electron energy loss spectroscopy (EELS) elemental mapping of the *ac*-plane shows a well-defined distribution of Fe, Ga, and Te in excellent agreement with the structure revealed by the HAADF image (Figure 1h). These STEM results further confirm the proposed crystal structure and demonstrate the high quality of the as-synthesized c-Fe_3GaTe_2 crystal.

2.2. Ferromagnetic Properties of c-Fe_3GaTe_2 Bulk Crystals and Nanosheets

The temperature-dependent magnetization (*M*–*T*) measurements, conducted using zero-field-cooling and field-cooling procedures, show a typical ferromagnetic–paramagnetic transition at 356 K under an applied field of 0.1 T along the *c*-axis. This transition indicates that the T_c of c-Fe_3GaTe_2 is significantly above the room temperature (**Figure 2**a). The magnetic-field-dependent magnetization (*M*–*H*) curves along the *c*-axis demonstrate clear hysteresis loops with a saturation field of 0.65 T at 2 K (Figure 2b). By contrast, the *M*–*H* curves along the *ab*-plane do not show hysteresis or saturation even under an applied magnetic field up to 7 T at 2 K (Figure 2c). This behavior indicates that the c-Fe_3GaTe_2 possesses a large perpendicular magnetic anisotropy, with the *c*-axis being the easy magnetization direction. The *M*–*H* curves of c-Fe_3GaTe_2 at the various temperatures under applied magnetic fields along the *c*-axis and *ab*-plane reveal that the saturation magnetization of Fe_3GaTe_2 gradually decreases with increasing temperature, yet remains ferromagnetic behavior up to 350 K, further indicating the high T_c of c-Fe_3GaTe_2.

Electrical transport measurements were carried out to investigate the intrinsic ferromagnetic properties of c-Fe_3GaTe_2 nanosheets. As shown in Figure 2d, a piece of c-Fe_3GaTe_2 nanosheet with a uniform thickness of 12 nm (corresponding to 15 layers) was peeled off and transferred onto a preprepared Hall electrode (device #1), and its longitudinal Hall resistance R_{xx} and transverse Hall resistance R_{xy} were measured separately. The R_{xx} in device #1 exhibits a symmetrical butterfly shaped hysteresis when an external magnetic field is applied perpendicular to the *ab*-plane (Figure 2e), whereas the R_{xy} shows a near square-shaped hysteresis loop with a large coercivity of 1.7 T (Figure 2f). The measured Hall resistance R_{xy} includes both a normal Hall resistance signal and an anomalous Hall resistance (AHR) signal.[15] However, in the metallic ferromagnetic material c-Fe_3GaTe_2, the normal Hall resistance is negligible compared to the AHR. Therefore, the R_{xy} can be predominantly attributed to the AHR, which is proportional to the magnetic moment (*M*) of the sample. The R_{xy} in device #1 maintains its nonlinear behavior up to 350 K, demonstrating the robust room-temperature long-range ferromagnetic order in few-layer c-Fe_3GaTe_2 nanosheets. Additionally, the thickness-dependent R_{xy} in c-Fe_3GaTe_2 devices (Figure 2h) shows that the coercivity and saturation fields in R_{xy} decrease with the increasing thicknesses of c-Fe_3GaTe_2 nanosheets, suggesting the highly thickness-dependent magnetic properties in c-Fe_3GaTe_2 nanosheets.

To directly observe the thickness-dependent magnetic domain structures in c-Fe_3GaTe_2, a nanosheet with varying thickness regions was exfoliated and transferred onto a SiO_2/Si substrate (Figure 2i). The thickness-dependent magnetic domain structures of the c-Fe_3GaTe_2 nanosheet were directly imaged at room temperature using a magnetic force microscope (MFM), without the applied magnetic field. The strong MFM signals confirm that the c-Fe_3GaTe_2 nanosheet has strong spontaneous magnetizations at room temperature, further reinforcing the evidence of its robust room-temperature ferromagnetic property (Figure 2g). In addition, the c-Fe_3GaTe_2 nanosheet displays distinct magnetic domain structures across areas of different thicknesses. In thicker regions, labyrinthian domain structures are observed, similar to those in ferromagnetic thin films with strong perpendicular magnetization.[16] Such patterns are proposed to stem from the dominant contribution of dipolar interactions during the spontaneous magnetization process. However, as the thickness decreases, these labyrinthian domains gradually become

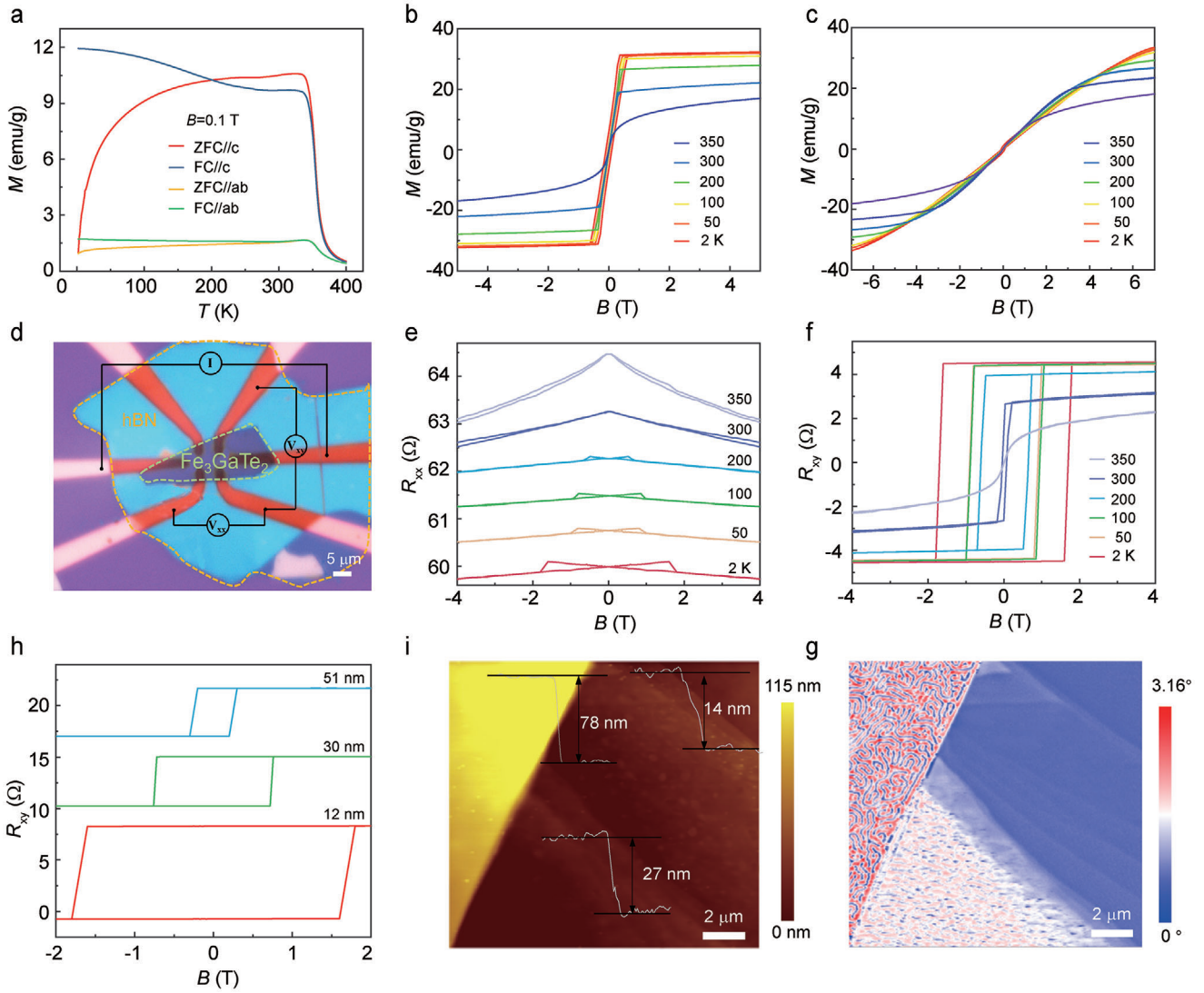

Figure 2. a) Temperature-dependent magnetization curves of the as-grown c-Fe_3GaTe_2 bulk crystal, measured in a 0.1 T external field along both the *c*-axis and the *ab*-plane. The Curie temperature was determined to be 356 K. b) Field-dependent magnetization plot of c-Fe_3GaTe_2 at varying temperatures, under a magnetic field along the *c*-axis of the crystal. c) Field-dependent magnetization plot of c-Fe_3GaTe_2 at varying temperatures, under a magnetic field along the *ab*-plane of the crystal. d) Optical image of the uniformly thick c-Fe_3GaTe_2 device (device #1). The green dash outlines the c-Fe_3GaTe_2 layer, and the yellow dash demarcates the top h-BN layer. e,f) Magnetic field dependence of the R_{xx} (e) and R_{xy} (f) in the device #1 at various temperatures, with the magnetic field perpendicular to the surface of the nanodevice. g) MFM imaging of the magnetic domain structures in the c-Fe_3GaTe_2 nanosheet with different thickness areas, conducted at room temperature without an applied magnetic field. h) Thickness-dependent anomalous Hall effect observed in the device #1. i) The distinct thicknesses in a c-Fe_3GaTe_2 nanosheet exfoliated onto the SiO_2/Si substrate were measured by AFM.

fragmented and evolve into single domain structures in thinner areas, indicating that the exchange interaction energy and the magnetocrystalline anisotropy energy gradually become dominant over the dipolar interaction energy.

2.3. Room-Temperature Antisymmetric Magnetoresistance in c-Fe_3GaTe_2 Nanosheets

In contrast to device #1, device #2 was constructed by transferring an exfoliated c-Fe_3GaTe_2 nanosheet with varying thicknesses onto two sets of Hall electrodes. A step edge separates the c-Fe_3GaTe_2 nanosheet into a thicker region (29 nm) and a thinner region (12 nm) (device #2) (**Figure** 3a). Measurements of the R_{xx} and R_{xy} across the step edge were conducted at 300 K, with an applied magnetic field perpendicular to the *ab*-plane (Figure 3b). The R_{xx} across the step edge in device #2 shows an unconventional antisymmetric MR, displaying three distinct resistance states (high, intermediate, and low), while the R_{xy} presents a tailed hysteresis loop. Moreover, the magnetic fields at which the antisymmetric peak appears ($Peak_A$), and disappears ($Peak_D$) are identified at 210 and 800 Oe, respectively, corresponding to the magnetic field changes during the magnetization reversal as observed in R_{xy}.

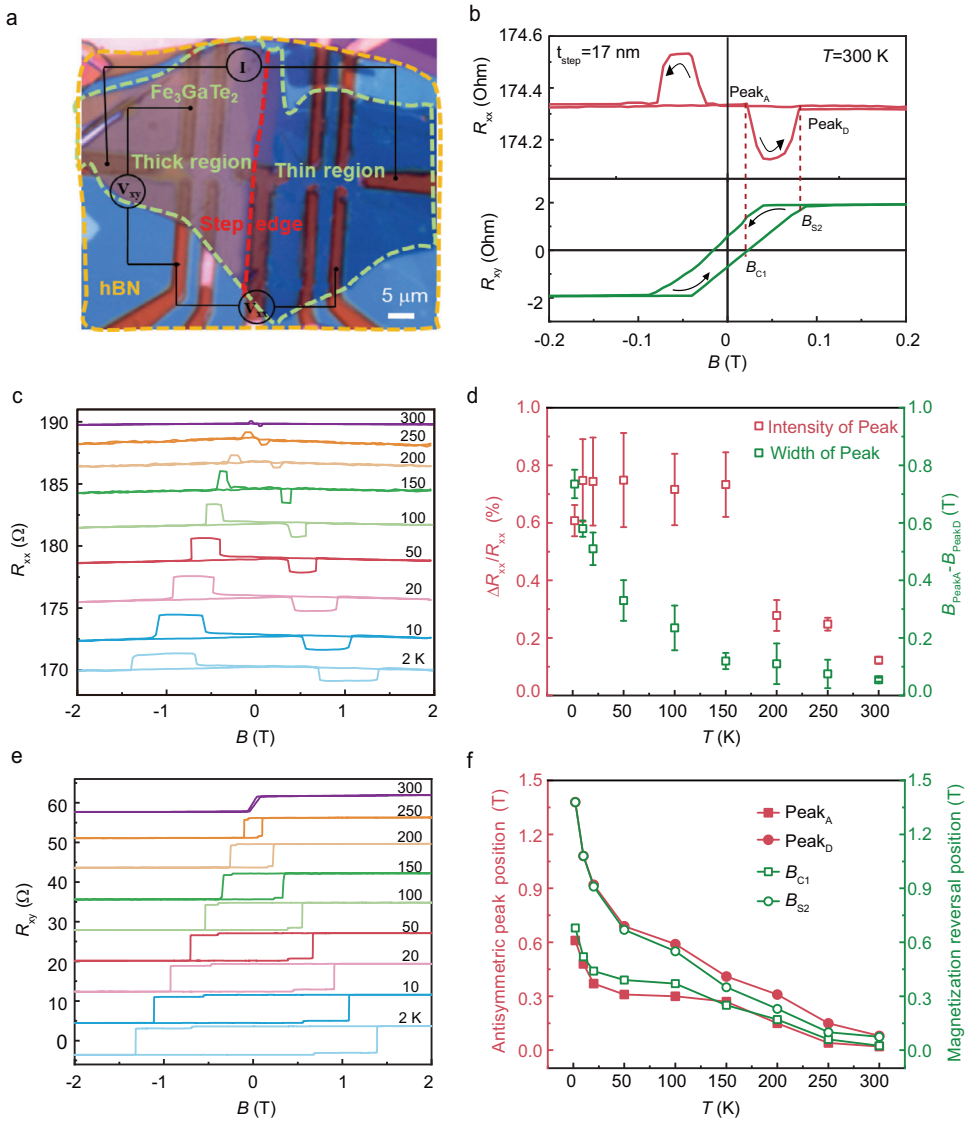

Figure 3. a) Optical image of the c-Fe_3GaTe_2 device (device #2) with two sets of Hall electrode configurations and varying thicknesses. The green dash outlines the c-Fe_3GaTe_2 layer, the red dash separates the thin and thick regions (step edge), the yellow dash defines the top h-BN layer, and the black lines mark the measured configurations. b) Field dependence of the R_{xx} and R_{xy} in device #2 at 300 K. The black arrow indicates the direction of magnetization flipping, and the red dash marks the corresponding positions of R_{xx} and R_{xy}. The positions of the magnetic field where the antisymmetric peak appears and disappears are defined as $Peak_A$ and $Peak_D$, respectively. The positions of the first coercive field and the second saturation field are defined as B_{C1} and B_{S2}, respectively. c) Field dependence of R_{xx} at varying temperatures in device #2 under a magnetic field perpendicular to the *ab*-plane of the device. d) The intensity and width of the peak at different temperatures, extracted from (c). e) Field dependence of R_{xy} at varying temperatures in device #2, under a magnetic field perpendicular to the *ab*-plane of the device. f) The positions of the antisymmetric peak in R_{xx} and the positions of magnetization reversal in R_{xy} as a function of temperature extracted from (c, e).

To further investigate the antisymmetric MR and magnetization switching, temperature-dependent measurements of R_{xx} and R_{xy} across the step edge in device #2 were performed. Over the temperature range of 2–300 K, the R_{xx} exhibits a broad antisymmetric plateau with sharp transitions (Figure 3c), and the corresponding R_{xy} shows step-like features (Figure 3e). The intensity and the width of antisymmetric plateau extracted from Figure 3c show a monotonic decrease with increasing temperature (Figure 3d). Additionally, the magnetic fields for the antisymmetric peak in R_{xx} significantly overlap the magnetic fields for magnetization reversal in the corresponding R_{xy} at various temperatures, also showing a monotonic decrease with increasing temperature (Figure 3f).

Additional experiments were conducted to understand the relationship between the observed antisymmetric MR and the magnetization evolution of c-Fe_3GaTe_2. Separate measurements of R_{xx} and R_{xy} in the thin, thick, and step-edge regions in device #2 were performed using different electrode probes during magnetization reversal (Figure S6a, Supporting Information). The R_{xx} in the step-edge region exhibits an antisymmetric behavior,

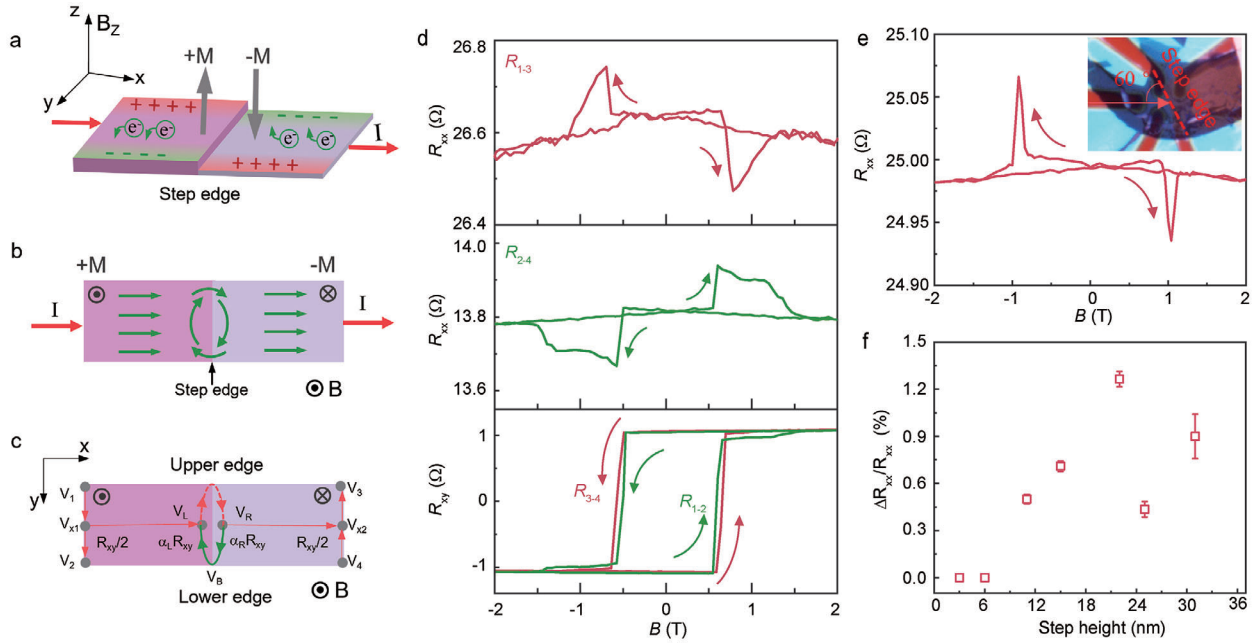

Figure 4. a) Schematic illustration of the distinct magnetization states corresponding to different thicknesses. The red arrows indicate the direction of the current, and the applied magnetic field is along the *z*-axis. Electrons are reflected on one side of the sample. b) A circulating current is observed around the step edge between the two regions with different magnetization states. c) The model of the circulating current, with red arrows indicating the direction of the electric fields. d) The R_{xx} measured at the upper edge across V_1 and V_3 and the lower edge across V_2 and V_4 at 2 K, shows opposite polarity with the same current from I_1 to I_2. The R_{xy} measured from the left edge across V_1 and V_2 (green line) and the right edge across V_3 and V_4 (red line) (device #3). e) The R_{xx} of the c-Fe_3GaTe_2 device with a tilting step edge (device #4) was measured at 2 K, with the optical image shown in the right of the inset. f) The step-height-dependent intensity of antisymmetric MR in diverse devices at 2 K.

while the R_{xx} in the thick and thin regions present symmetrical butterfly shaped loops (Figure S6b, Supporting Information). Moreover, the magnetic fields at which the antisymmetric MR appears and disappears correspond to the magnetic fields of the highest points of the butterfly curves for the thick and thin regions where the magnetic moment flipping occurs. The R_{xy} in the step-edge region shows two sharp transitions at 0.71 and 1.31 T, corresponding to the coercive fields of thick and thin regions, respectively, suggesting the presence of unsynchronized magnetization switching in device #2 during sweeping the magnetic field (Figure S6c, Supporting Information). Apart from the magnetic field of antisymmetric MR coinciding with the coercive field where the R_{xy} magnetization reverses, the magnitude of antisymmetric MR is consistent with the difference of the saturation magnetic moment between the thick and thin regions. These results suggest that the appearance of the antisymmetric MR originates from the AHR of the c-Fe_3GaTe_2, which results from unsynchronized magnetization switching in the c-Fe_3GaTe_2 devices with a step structure that breaks the planar symmetry.

There are two possible scenarios for the observed antisymmetric MR, which are as follows. 1) In magnetic thin films with perpendicular anisotropy, two single magnetic domains separated by a domain wall are formed. When a current is passed perpendicularly through the domain wall, anomalous Hall effect generates a circulating current in the vicinity of the domain walls, which contributes to R_{xx}. 2) In the magnetic heterostructures, the unsynchronized magnetization switching has a strong correlation with the spin-momentum locking induced by Rashba spin orbit coupling at the interface. In this scenario, the current direction determining electron spin polarization of the spin current may coincide with or be opposite to the direction of the magnetization in one ferromagnetic layer, which leads to different resistive states. In our experiment, the Fe_3GaTe_2 exhibits the large perpendicular anisotropy, and the uneven thickness of Fe_3GaTe_2 nanosheets can lead to the appearance of magnetic domain walls, consistent with the structural characteristics of the first scenario. Therefore, the antisymmetric MR observed in our experiment is similar with the phenomenon seen in magnetic multilayers with perpendicular anisotropy, where unsynchronized magnetization switching in AHR induces a circulating current across the domain walls, thereby contributing to R_{xx}.[17] As schematically illustrated in **Figure** 4a, the c-Fe_3GaTe_2 nanosheet with varying thicknesses is separated into two parts: a thicker region on the left, and a thinner region on the right. Correspondingly, the thicker region has a larger saturation magnetization than the thinner region. When the magnetic field is swept from −2 to 2 T (upward), at high negative fields exceeding the saturation magnetic field of both the thick and thin Fe_3GaTe_2 nanosheets, the magnetic moments in both regions align along the direction of the applied negative field. When the applied magnetic field is altered to reach the positive saturation magnetic field of the thick region, the magnetization of the thick region reverses due to its perpendicular magnetic anisotropy, while the magnetization of the thin region remains aligned with the negative magnetic field. This results in the formation of a magnetic domain wall around the step edge during magnetization reversal. In this scenario, the opposite magnetizations along the *z*-axis in the thick and thin regions induce disparate anomalous velocities in the moving electrons

along the *x*-axis. Consequently, electrons in the two regions, characterized by different thicknesses, undergo deflection in distinct directions along the *y*-axis, thereby generating a circulating current around the step edge to maintain the continuity of the current field (Figure 4b). The spatial distribution of the circulating current is intricately linked to the configuration of magnetic moments within the regions of varying thicknesses. Therefore, as the magnetic field is swept downward, the distribution of the circulating current changes accordingly. This varying current contributes differently to the R_{xx} with the sweeping of the magnetic field, resulting in the observed antisymmetric behavior in R_{xx}.

To elucidate the mechanism behind the antisymmetric MR behavior, we quantitatively analyzed the actual R_{xx} based on the distribution of the circular current (the details of the calculation process can be found in Note S2 in the Supporting Information). As shown in Figure 4c, the applied current flows along the *x*-axis. The longitudinal voltage on the upper edge is measured using probes V_1 and V_3, while the longitudinal voltage on the lower edge is measured with probes V_2 and V_4. Taking the lower voltage as an example, the resistance R_{2-4} can be calculated as

$$R_{2-4} = R_{xx-int} + R_{xy-C} + \alpha_L R_{xy} + \alpha_R R_{xy} \quad (1)$$

Here, the measured R_{2-4} is composed of three parts: the intrinsic MR $R_{xx\text{-int}}$, a component of $R_{xy\text{-C}}$, and the perturbation caused by the circulating current near the step edge $\alpha_L R_{xy} + \alpha_R R_{xy}$. After deducting the intrinsic MR $R_{xx\text{-int}}$ and the contribution from $R_{xy\text{-C}}$, the remaining antisymmetric MR can be written as

$$\Delta R_{2-4} = \alpha_L R_{xy} + \alpha_R R_{xy} \quad (2)$$

When the field is swept upward, the antisymmetric MR is written as

$$\Delta R_{2-4}(+) = \alpha_L R_{xy}(+) + \alpha_R R_{xy}(+) \quad (3)$$

By contrast, when the field is reversed, the magnetizations in the thick and thin regions are reversed accordingly

$$\Delta R_{2-4}(-) = -\alpha_L R_{xy}(+) - \alpha_R R_{xy}(+) = -\Delta R_{2-4}(+) \quad (4)$$

This relationship accounts for the antisymmetric behavior of the longitudinal MR. During the magnetization reversal, the direction of the circulating current in the upper edge is always opposite to that at the lower step edge, resulting in opposite polarity of antisymmetric MR between R_{1-3} and R_{2-4}. Consequently, the R_{1-3} in the upper edge and R_{2-4} in the lower edge of device #3 were measured utilizing different measurement configurations (Figure 4d). The opposite sign of antisymmetric MRs in the upper and lower edge confirms that the antisymmetric MR is caused by a circulating current in the vicinity of the domain walls.

In contrast to other 2D systems where antisymmetric MR is observed only at low temperatures,[11–13] the room-temperature antisymmetric MR in c-Fe_3GaTe_2 nanosheets shows great potential for application in 2D spintronic devices. Therefore, exploring the factors influencing this antisymmetric MR is crucial for optimizing the device performance and achieving control over the antisymmetric MR. Originally, models of antisymmetric MR required that the single domain wall, current, and magnetization direction must be perpendicular to each other.[17,18] However, later observations also identified antisymmetric MR in structures with tilted magnetic domain walls.[13a,19] To investigate the relationship between the directions of current, domain wall, and magnetization in the thickness-inhomogeneous c-Fe_3GaTe_2 devices, we constructed a device (device #4) with an ≈60° angle between the current direction and the step edge. As shown in Figure 4e, the observation of antisymmetric MR in device #4 supports the idea that tilted magnetic domain walls can also give rise to antisymmetric MR.

We further study the effect of step height on antisymmetric MR, considering its relation to the difference in AHR between thin and thick regions. Several devices with distinct step height were constructed, while maintaining the thickness of the thin regions at ≈12 nm. Interestingly, the antisymmetric MR did not show a monotonic variation with step height (Figure 4f). The intensity of the antisymmetric MR peaked at a step height of 22 nm and disappeared at a reduced step height of 6 nm, where the difference in AHR between thick and thin regions becomes negligible.

According to the proposed model, the circulating current near the boundary of the domain walls between regions with various thicknesses contributes to the longitudinal MR, leading to the antisymmetric behavior. Therefore, we carried out additional experiments to study the effect of domain wall dynamics. When the magnetic field sweeps back and forth, a domain wall between two regions with different thicknesses is formed. The slower field sweep rates can result in the gradual formation and evolution of magnetic domain walls, while the faster sweep rates lead to magnetic domain walls' rapidly forming and annihilating. Because the circulating current near the boundary of the domain walls gives rise to the antisymmetric behavior in the longitudinal MR, the faster sweep rates can smooth the shape of the antisymmetric MR and narrow the width of the peak. As shown in Figure S9 (Supporting Information), measurements of the magnetic-field-dependent MR at various sweep rates show that slower scanning speeds led to broader peaks. However, the peak height of the antisymmetric MR is only determined by the difference of the saturated magnetization between the two regions, and is independent of the sweep rates. Therefore, the height of the antisymmetric MRs under various sweep rates remained unchanged. In addition, we also investigated the influence of the applied current on the antisymmetric MR. As shown in Figure S10 (Supporting Information), the shape and magnitude of the peak remained nearly unchanged under the different applied currents, suggesting that the magnitude of the generated circulating current is determined solely by the intrinsic AHR of the c-Fe_3GaTe_2 nanosheets, and not by the applied external current. Therefore, the room-temperature antisymmetric MR in c-Fe_3GaTe_2 nanosheets can be measured with a small applied current. This characteristic offers tremendous potential for developing ultralow-power storage and logic devices, providing a significant advantage over devices based on spin orbit torque and spin transfer torque.[20]

3. Conclusions

In conclusion, we successfully synthesized high-quality, room-temperature ferromagnetic c-Fe_3GaTe_2 single crystals by the CVT method. Room-temperature antisymmetric MR was observed in

c-Fe_3GaTe_2 devices featuring a step structure that breaks the planar symmetry. Through comprehensive studies of temperature-, current-, step-thickness-, and scanning-rate-dependent MR, we reveal the relationship between the magnetization evolution and the observed antisymmetric MR. Due to the thickness-dependent AHR, the unsynchronized magnetic switching appears in c-Fe_3GaTe_2 devices with inhomogeneous thickness. Consequently, the circulating current near the boundary of the domain walls contributes to the longitudinal MR, giving rise to the antisymmetric behavior in the longitudinal MR when the magnetic field sweeps back and forth. The magnitude of the antisymmetric MR is solely determined by the thickness-dependent AHR and can be regulated and optimized by controlling the step height between the thin and thick regions. The high-quality, room-temperature ferromagnetic c-Fe_3GaTe_2 with strong perpendicular magnetic anisotropy shows immense potential for the application in 2D spintronic devices. Moreover, the unconventional room-temperature antisymmetric MR demonstrates three resistance states – high, intermediate and low – which possess great advantages in low-power random storage and logic circuits.

4. Experimental Section

Single Crystal Growth: The Fe_3GaTe_2 single crystals were grown by two methods: the CVT and self-flux. The CVT growth process began with a mixture of Fe power (99.95%), Ga pellet (99.9999%), and Te lump (99.999%) in a stoichiometric molar ratio of 3:1:2, prepared in an Ar-filled glove box. Subsequently, the mixture and an amount of the transport agent NH_4Cl were sealed together into an evacuated quartz tube. The sealed quartz tube was then placed in a two-zone tubular furnace. The temperatures were ramped to 880/780 °C with 2 °C min^{-1}, maintained at 880/780 °C for two weeks, and then cooled to room temperature naturally. Finally, a hexagonal Fe_3GaTe_2 single crystal with a metallic luster was obtained.

The Fe_3GaTe_2 single crystals were also grown by the Te self-flux method, as described in ref. [14]. A mixture of Fe power (99.95%), Ga pellet (99.9999%), and Te lump (99.999%) was prepared in a stoichiometric molar ratio of 1:2:2 in an Ar-filled glove box. The mixture was transferred into an alumina crucible, and then the crucible containing the mixture was placed into an evacuated quartz tube. The quartz tube was sealed, and then placed into a vertical furnace to react. The temperature was ramped to 1000 °C within 1 h, and kept at 1000 °C for 24 h. Then, the mixture was rapidly cooled to 880 °C within 1 h, and then gradually cooled down to 780 °C within 100 h. Finally, the quartz tube at 780 °C was removed to centrifuge for removing the excess flux.

Structural and Elemental Analysis: The phase purity of the single crystal was analyzed by powder X-ray diffraction with the Cu Kα radiation. Single crystal X-ray diffraction (Bruker D8 Venture) was used to examine the (0*kl*) plane diffraction pattern of Fe_3GaTe_2 grown by the CVT and self-flux. Scanning electron spectroscopy (SEM) equipped with EDS was utilized to determine the stoichiometric ratio. Specimens for STEM were prepared by the focused ion beam, and STEM characterization was performed on an aberration-corrected JEOL GRANDARM2 operated at 200 kV. The beam convergence semiangle was 32 mrad, and the collection semiangles were 68–280 mrad for HAADF images and 17 mrad for ABF images, respectively. For the EELS analysis, the convergence semiangle was 32 mrad and the collection semiangle was 45 mrad. The EELS elemental mapping results were denoised by performing principal component analysis for each element individually.

Magnetic Measurement: The magnetization of the single crystal was measured by a superconducting quantum interference device (SQUID) (Quantum Design MPMS-3). A commercial Cypher S Atomic Force Microscopy (AFM) (Oxford Instruments, Asylum Research, Santa Barbara, USA) was used to determine the thickness of Fe_3GaTe_2 nanosheets, and measure the magnetic domain structures of Fe_3GaTe_2 nanosheets at room temperature under zero magnetic field by equipping with a commercial magnetic tip (nanosensors, PPP-MFMR-10, force constant: 0.5–9.5 N m^{-1}, resonance frequency: ≈65 kHz). The MFM images were captured in a two-pass imaging mode, where the topography was recorded in the first pass for each scanned line, and then the tip was raised 200 nm above the surface to image the magnetic forces in the second pass.

Device Fabrication: The contact electrodes with the different configurations were prefabricated by the ultraviolet lithography, magnetron sputtering, and lift-off process. The c-Fe_3GaTe_2 single crystal was mechanically exfoliated by the magic Scotch tape. Then, a suitable c-Fe_3GaTe_2 nanosheet was transferred onto the prefabricated Hall bar electrodes using polydimethylsiloxane. To protect the nanosheet, a layer of hexagonal boron nitride (hBN) was transferred to cover it. All the exfoliation and transfer processes were carried out in an Ar-filled glove box (H_2O, $O_2 < 0.1$ ppm).

Magnetotransport Measurements: The electrical transport measurements were carried out in a physical property measurement system (DynaCool, Quantum Design) with a standard four-terminal configuration. The temperature could be accurately controlled down to 1.9 K. The magnetic field ranged from −16 to 16 T.

Data Processing: The data processing for antisymmetric MRs could refer to the refs. [12b,13a]. Typically, the Hall resistance data could be processed by using $R_{xy}(+B) - R_{xy}(-B)/2$ to eliminate the contribution from the longitudinal MR, and the longitudinal MR data could be processed by using $R_{xx}(+B) + R_{xx}(-B)/2$ to eliminate the contribution from the Hall resistance. However, because of the antisymmetric features in the longitudinal MR, the measured R_{xx} could not be processed by using $R_{xx}(+B) + R_{xx}(-B)/2$ to eliminate the contribution from the Hall resistance, the magnetic hysteresis loop observed in the longitudinal MR originated from the contribution of the Hall resistance. Therefore, the loop was subtracted from the R_{xx} raw data to eliminate the effect of the Hall resistance. The R_{xx} raw data are shown in the Supporting Information. Regarding the measured R_{xx} without antisymmetric features, the data were processed by using $R_{xx}(+B) + R_{xx}(-B)/2$ to eliminate the contribution from the Hall resistance.

Supporting Information

Supporting Information is available from the Wiley Online Library or from the author.

Acknowledgements

The work was supported by grants from the National Key Research and Development Projects of China (Grant No. 2022YFA1204104), the National Natural Science Foundation of China (Grant No. 61888102), the Chinese Academy of Sciences (Grant Nos. XDB33030100, ZDBS-SSW-WHC001), the Innovation Program of Quantum Science and Technology (Grant No. 2021ZD0302700), and the CAS Project for Young Scientists in Basic Research (Grant No. YSBR-003). This research benefited from resources and supports from the Electron Microscopy Center at the University of Chinese Academy of Sciences.

Conflict of Interest

The authors declare no conflict of interest.

Author Contributions

G.J.H. and H.G. contributed equally to this work. H.T.Y. and H.-j.G. designed the project. G.J.H. and H.G. prepared the samples, performed the electrical transport measurements, and worked with the data. S.H.L. performed the SQUID measurements. L.X.L., J.A.S., and W.Z. performed the measurement and analysis of STEM. Y.H.W. and S.Y.Z. performed the

MFM measurements. Y.C.H. and X.L. performed the SEM measurements. L.L.P. performed the XRD measurement. Y.L.X. and W.Q.Y. performed the AFM measurements. K.Z. and L.H.B. performed the processing of micro-/nanometal electrodes. Q.Q. and G.Y.X. provided support in data analysis. All authors participated in the data analysis and paper writing.

Data Availability Statement

The data that support the findings of this study are available from the corresponding author upon reasonable request.

Keywords

antisymmetric magnetoresistance, Fe_3GaTe_2, planar symmetry breaking, room-temperature, van der Waals ferromagnet

Received: March 1, 2024
Revised: April 8, 2024
Published online:

[1] a) M. Gibertini, M. Koperski, A. F. Morpurgo, K. S. Novoselov, *Nat. Nanotechnol.* **2019**, *14*, 408; b) C. Gong, X. Zhang, *Science* **2019**, *363*, 706; c) C. Dai, P. He, L. Luo, P. Zhan, B. Guan, J. Zheng, *Sci. China Mater.* **2023**, *66*, 859.

[2] a) C. Gong, L. Li, Z. Li, H. Ji, A. Stern, Y. Xia, T. Cao, W. Bao, C. Wang, Y. Wang, Z. Q. Qiu, R. J. Cava, S. G. Louie, J. Xia, X. Zhang, *Nature* **2017**, *546*, 265; b) B. Huang, G. Clark, E. Navarro-Moratalla, D. R. Klein, R. Cheng, K. L. Seyler, D. Zhong, E. Schmidgall, M. A. McGuire, D. H. Cobden, W. Yao, D. Xiao, P. Jarillo-Herrero, X. Xu, *Nature* **2017**, *546*, 270; c) Y. Deng, Y. Yu, Y. Song, J. Zhang, N. Z. Wang, Z. Sun, Y. Yi, Y. Z. Wu, S. Wu, J. Zhu, J. Wang, X. H. Chen, Y. Zhang, *Nature* **2018**, *563*, 94.

[3] a) H. Li, S. Ruan, Y. J. Zeng, *Adv. Mater.* **2019**, *31*, 1900065; b) K. S. Burch, D. Mandrus, J. G. Park, *Nature* **2018**, *563*, 47.

[4] a) Z. Fei, B. Huang, P. Malinowski, W. Wang, T. Song, J. Sanchez, W. Yao, D. Xiao, X. Zhu, A. F. May, W. Wu, D. H. Cobden, J. H. Chu, X. Xu, *Nat. Mater.* **2018**, *17*, 778; b) S. Jiang, J. Shan, K. F. Mak, *Nat. Mater.* **2018**, *17*, 406; c) Z. Wang, T. Zhang, M. Ding, B. Dong, Y. Li, M. Chen, X. Li, J. Huang, H. Wang, X. Zhao, Y. Li, D. Li, C. Jia, L. Sun, H. Guo, Y. Ye, D. Sun, Y. Chen, T. Yang, J. Zhang, S. Ono, Z. Han, Z. Zhang, *Nat. Nanotechnol.* **2018**, *13*, 554; d) D. Ghazaryan, M. T. Greenaway, Z. Wang, V. H. Guarochico-Moreira, I. J. Vera-Marun, J. Yin, Y. Liao, S. V. Morozov, O. Kristanovski, A. I. Lichtenstein, M. I. Katsnelson, F. Withers, A. Mishchenko, L. Eaves, A. K. Geim, K. S. Novoselov, A. Misra, *Nat. Electron.* **2018**, *1*, 344.

[5] a) A. F. May, D. Ovchinnikov, Q. Zheng, R. Hermann, S. Calder, B. Huang, Z. Fei, Y. Liu, X. Xu, M. A. McGuire, *ACS Nano* **2019**, *13*, 4436; b) X. Lv, K. Pei, C. Yang, G. Qin, M. Liu, J. Zhang, R. Che, *ACS Nano* **2022**, *16*, 19319; c) F. M. Oliveira, N. Antonatos, V. Mazánek, D. Sedmidubský, Z. Sofer, R. Gusmão, *FlatChem* **2022**, *32*, 100334; d) A. V. Papavasileiou, M. Menelaou, K. J. Sarkar, Z. Sofer, L. Polavarapu, S. Mourdikoudis, *Adv. Funct. Mater.* **2024**, *34*, 2309046.

[6] a) X. Sun, W. Li, X. Wang, Q. Sui, T. Zhang, Z. Wang, L. Liu, D. Li, S. Feng, S. Zhong, H. Wang, V. Bouchiat, M. Nunez Regueiro, N. Rougemaille, J. Coraux, A. Purbawati, A. Hadj-Azzem, Z. Wang, B. Dong, X. Wu, T. Yang, G. Yu, B. Wang, Z. Han, X. Han, Z. Zhang, *Nano Res.* **2020**, *13*, 3358; b) M. Huang, S. Wang, Z. Wang, P. Liu, J. Xiang, C. Feng, X. Wang, Z. Zhang, Z. Wen, H. Xu, G. Yu, Y. Lu, W. Zhao, S. A. Yang, D. Hou, B. Xiang, *ACS Nano* **2021**, *15*, 9759; c) L. Meng, Z. Zhou, M. Xu, S. Yang, K. Si, L. Liu, X. Wang, H. Jiang, B. Li, P. Qin, P. Zhang, J. Wang, Z. Liu, P. Tang, Y. Ye, W. Zhou, L. Bao, H. J. Gao, Y. Gong, *Nat. Commun.* **2021**, *12*, 809.

[7] a) W. Han, *APL Mater.* **2016**, *4*, 032401; b) G. Hu, B. Xiang, *Nanoscale Res. Lett.* **2020**, *15*, 226.

[8] K. F. Mak, J. Shan, D. C. Ralph, *Nat. Rev. Phys.* **2019**, *1*, 646.

[9] a) T. Song, X. Cai, M. W.-Y. Tu, X. Zhang, B. Huang, N. P. Wilson, K. L. Seyler, L. Zhu, T. Taniguchi, K. Watanabe, M. A. McGuire, D. H. Cobden, D. Xiao, W. Yao, X. Xu, *Science* **2018**, *360*, 1214; b) Z. Wang, I. Gutierrez-Lezama, N. Ubrig, M. Kroner, M. Gibertini, T. Taniguchi, K. Watanabe, A. Imamoglu, E. Giannini, A. F. Morpurgo, *Nat. Commun.* **2018**, *9*, 2516; c) Z. Wang, D. Sapkota, T. Taniguchi, K. Watanabe, D. Mandrus, A. F. Morpurgo, *Nano Lett.* **2018**, *18*, 4303; d) H. Lin, F. Yan, C. Hu, Q. Lv, W. Zhu, Z. Wang, Z. Wei, K. Chang, K. Wang, *ACS Appl. Mater. Interfaces* **2020**, *12*, 43921; e) W. Jin, G. Zhang, H. Wu, L. Yang, W. Zhang, H. Chang, *ACS Appl. Mater. Interfaces* **2023**, *15*, 36519; f) W. Jin, G. Zhang, H. Wu, L. Yang, W. Zhang, H. Chang, *Nanoscale* **2023**, *15*, 5371.

[10] a) M. N. Baibich, J. M. Broto, A. Fert, F. Nguyen Van Dau, F. Petroff, P. Etienne, G. Creuzet, A. Friederich, J. Chazelas, *Phys. Rev. Lett.* **1988**, *61*, 2472; b) S. S. Parkin, C. Kaiser, A. Panchula, P. M. Rice, B. Hughes, M. Samant, S. H. Yang, *Nat. Mater.* **2004**, *3*, 862; c) S. Yuasa, T. Nagahama, A. Fukushima, Y. Suzuki, K. Ando, *Nat. Mater.* **2004**, *3*, 868.

[11] Q. L. He, G. Yin, L. Yu, A. J. Grutter, L. Pan, C. Z. Chen, X. Che, G. Yu, B. Zhang, Q. Shao, A. L. Stern, B. Casas, J. Xia, X. Han, B. J. Kirby, R. K. Lake, K. T. Law, K. L. Wang, *Phys. Rev. Lett.* **2018**, *121*, 096802.

[12] a) S. Albarakati, C. Tan, Z.-J. Chen, J. G. Partridge, G. Zheng, L. Farrar, E. L. H. Mayes, M. R. Field, C. Lee, Y. Wang, Y. Xiong, M. Tian, F. Xiang, A. R. Hamilton, O. A. Tretiakov, D. Culcer, Y.-J. Zhao, L. Wang, *Sci. Adv.* **2019**, *5*, eaaw0409; b) G. Hu, Y. Zhu, J. Xiang, T. Y. Yang, M. Huang, Z. Wang, Z. Wang, P. Liu, Y. Zhang, C. Feng, D. Hou, W. Zhu, M. Gu, C. H. Hsu, F. C. Chuang, Y. Lu, B. Xiang, Y. L. Chueh, *ACS Nano* **2020**, *14*, 12037; c) Q. Wu, Z. Cui, M. Zhu, Z. Jiang, Z. Fu, Y. Lu, *2D Mater.* **2023**, *10*, 025009.

[13] a) P. Liu, C. Liu, Z. Wang, M. Huang, G. Hu, J. Xiang, C. Feng, C. Chen, Z. Ma, X. Cui, H. Zeng, Z. Sheng, Y. Lu, G. Yin, G. Chen, K. Liu, B. Xiang, *Nano Res.* **2021**, *15*, 2531; b) W. Niu, Z. Cao, Y. Wang, Z. Wu, X. Zhang, W. Han, L. Wei, L. Wang, Y. Xu, Y. Zou, L. He, Y. Pu, *Phys. Rev. B* **2021**, *104*, 125429.

[14] G. Zhang, F. Guo, H. Wu, X. Wen, L. Yang, W. Jin, W. Zhang, H. Chang, *Nat. Commun.* **2022**, *13*, 5067.

[15] E. M. Pugh, N. Rostoker, *Rev. Mod. Phys.* **1953**, *25*, 151.

[16] a) T. Guo, Z. Ma, X. Luo, Y. Hou, W. Meng, J. Wang, J. Zhang, Q. Feng, G. Lin, Y. Sun, Z. Sheng, Q. Lu, *Mater. Charact.* **2021**, *173*, 110913; b) R. Fujita, P. Bassirian, Z. Li, Y. Guo, M. A. Mawass, F. Kronast, G. van der Laan, T. Hesjedal, *ACS Nano* **2022**, *16*, 10545.

[17] a) X. M. Cheng, S. Urazhdin, O. Tchernyshyov, C. L. Chien, V. I. Nikitenko, A. J. Shapiro, R. D. Shull, *Phys. Rev. Lett.* **2005**, *94*, 017203; b) G. Xiang, A. W. Holleitner, B. L. Sheu, F. M. Mendoza, O. Maksimov, M. B. Stone, P. Schiffer, D. D. Awschalom, N. Samarth, *Phys. Rev. B* **2005**, *71*, 241307(R); c) W. Desrat, S. Kamara, F. Terki, S. Charar, J. Sadowski, D. K. Maude, *Semicond. Sci. Technol.* **2009**, *24*, 065011.

[18] G. Rodríguez-Rodríguez, J. L. Menéndez, A. Pérez-Junquera, A. Hierro-Rodriguez, N. Montenegro, D. Ravelosona, J. M. Alameda, M. Vélez, *J. Phys.: Conf. Ser.* **2010**, *200*, 042021.

[19] Y. Su, Y. Meng, H. Shi, L. Wang, X. Cao, Y. Zhang, R. Li, H. Zhao, *Phys. Rev. Appl.* **2022**, *17*, 014013.

[20] a) W. Li, W. Zhu, G. Zhang, H. Wu, S. Zhu, R. Li, E. Zhang, X. Zhang, Y. Deng, J. Zhang, L. Zhao, H. Chang, K. Wang, *Adv. Mater.* **2023**, *35*, 2303688; b) Z. C. Pan, D. Li, X. G. Ye, Z. Chen, Z. H. Chen, A. Q. Wang, M. Tian, G. Yao, K. Liu, Z. M. Liao, *Sci. Bull.* **2023**, *68*, 2743; c) H. Wang, H. Wu, J. Zhang, Y. Liu, D. Chen, C. Pandey, J. Yin, D. Wei, N. Lei, S. Shi, H. Lu, P. Li, A. Fert, K. L. Wang, T. Nie, W. Zhao, *Nat. Commun.* **2023**, *14*, 5173.